Solar Subsurface Fluid Dynamics Descriptors Derived from Global Oscillation Network Group and Michelson Doppler Imager Data

R. Komm, T. Corbard, B. Durney, I. Gonzalez Hernandez, F. Hill, R. Howe, C. Toner

SOLAR SUB-SURFACE FLUID DYNAMICS DESCRIPTORS DERIVED FROM GONG AND MDI DATA

R. Komm

National Solar Observatory[1],
950 N. Cherry Ave., Tucson, AZ 85719

T. Corbard

Observatoire de la Côte d'Azur, F-06304 Nice Cedex 4

B.R. Durney[2], I. González-Hernández, F. Hill, R. Howe, and C. Toner

National Solar Observatory
950 N. Cherry Ave., Tucson, AZ 85719

komm@noao.edu

ABSTRACT

We analyze GONG and MDI observations obtained during Carrington rotation 1988 (2002/3/30 - 2002/4/26) with a ring-diagram technique in order to measure the zonal and meridional flow components in the upper solar convection zone. We derive daily flow maps over a range of depths up to 16 Mm on a spatial grid of 7.5° in latitude and longitude covering ±60° in latitude and central meridian distance and combine them to make synoptic flow maps. We start exploring the dynamics of the near surface layers and the interaction between flows and magnetic flux by deriving fluid dynamics descriptors such as divergence and vorticity from these flow maps. Using these descriptors, we derive the vertical velocity component and the kinetic helicity. For this particular Carrington rotation, we find that the vertical velocity component is anticorrelated with the unsigned magnetic flux. Strong downflows are more likely associated with locations of strong magnetic activity. The vertical vorticity is positive in the northern and negative in the southern hemisphere. The presence of magnetic activity leads to an excess vorticity of the same sign as the one introduced by rotation. The vertical gradient of the zonal flow is mainly negative except within 2 Mm of the

[2]University of Arizona, Physics Department, Tucson, AZ 85721

surface at latitudes poleward of about 20°. The zonal-flow gradient appears to be related to the unsigned magnetic flux in the sense that locations of strong activity are also locations of large negative gradients. The vertical gradient of the absolute value of the meridional flow is mainly negative at depths greater than about 7 Mm and mainly positive closer to the surface. GONG and MDI data show the same results. Differences occur mainly at high latitudes especially in the northern hemisphere where MDI data show a counter cell in the meridional flow that is not present in the corresponding GONG data.

Subject headings: Sun: activity — Sun: helioseismology — Sun: magnetic fields — Sun: oscillations

1. INTRODUCTION

We study horizontal flows in the outer two percent of the Sun near the solar surface derived from GONG and MDI Doppler images using a ring-diagram analysis. The ring-diagram technique has been used with great success by Haber et al. (2000, 2002) to analyze MDI Dynamics-run data. They found that large-scale solar flows such as zonal and meridional flows are more complex in the presence of strong magnetic activity than during times of low activity. The most important results to come out of that analysis to date are the discovery and characterization of flow concentrations around active regions, and the structure of the near-surface global meridional circulation pattern, including a very surprising turnover at depths below about 7 Mm (counter cell) in the northern hemisphere only during the peak years of the solar activity cycle.

We start exploring the dynamics of the near surface layers of the convection zone by deriving fluid dynamics descriptors such as divergence (div $\mathbf{v}$) and vorticity (curl $\mathbf{v}$) from the measured horizontal flows. These descriptors allow us to estimate other quantities such as, for example, the vertical velocity component and the mean kinetic helicity. The kinetic helicity together with the magnetic helicity play an important role in solar dynamo models (Steenbeck & Krause 1966; Krause 1967; Dikpati & Gilman 2001; Kleeorin & Rogachevskii 2003). In addition, we derive the vertical gradients of the zonal flow (rotation) and the meridional flow, which is not only of interest for the understanding of the dynamics of the near surface layers but might also provide evidence for the existence of a near-surface

[1]Operated by the Association of Universities for Research in Astronomy, Inc. under cooperative agreement with the National Science Foundation.

dynamo. In this study, we focus on the relationship between these fluid dynamics descriptors and the magnetic flux to begin exploring more quantitatively the relation between dynamics and magnetic activity.

We show results from GONG and MDI observations covering Carrington rotation 1988 (2002/3/30 - 2002/4/26) analyzed with the GONG ring-diagram analysis pipeline (Corbard et al. 2003). The ring diagram technique uses 3-dimensional power spectra from small patches of the solar disk to follow zonal and meridional flows below the surface and monitor local near-surface changes in high-degree modes. Such analysis (Hill 1988) has previously been extensively used on the 'Dynamics' (full-field, 1024×1024 pixel) data from the MDI instrument aboard SOHO (Haber et al. 2000, 2002, for example). Upgraded cameras now allow similar data to be taken year-round from the six stations of the GONG network. Howe et al. (2003) shows results of an analysis of mode width and amplitudes obtained from such GONG data in addition to MDI data, while we focus in this study on the derived horizontal flows.

2. Data and Method

We analyze observations obtained during Carrington Rotation 1988 (March 30 – April 26, 2002), for which we have full-disc Doppler data from both the MDI instrument on SOHO and the GONG network. This data set was selected for the purposes of a detailed intercomparison of results obtained through multiple paths, from observation through each of the analysis steps. Such comparisons can provide a certain degree of validation of the implementations of the analysis procedures, hints of systematic errors, and better characterization of the observations, possibly leading to improved calibrations[3]. Bogart et al. (2003) discuss initial results of the on-going comparison with regard to the ring-diagram technique; a more detailed comparison is in preparation. In this study, we analyze both data sets with the GONG pipeline and compare the results to check their consistency and thus their reliability.

We determine the horizontal components of solar subsurface flows with a ring-diagram analysis. The underlying feature is that a local velocity field changes the frequencies of acoustic waves through the advection of the wave pattern (Gough & Toomre 1983). This shift can be measured by obtaining a time series of a localized area on the solar surface and then calculating a 3-dimensional power spectrum from this image cube as a function of temporal frequency, ω, and spatial frequencies, k_x and k_y (Hill 1988). A 2-dimensional cut

[3]For more information see the website of the Local Helioseismology Comparison Group at http://gong.nso.edu/lohco/.

at a given temporal frequency shows a set of rings where each one corresponds to a ridge in the $l - \nu$ diagram. These rings are shifted by the horizontal flow field in k_x and k_y. The rings are fitted to measure these shifts (Bogart et al. 1995) and these inferred shifts are then inverted to determine the horizontal velocity components.

We use the same technique as described by Haber et al. (2002) for their dense-pack analysis of MDI Dynamics Program data. We analyze the data in 'days' of 1664 minutes which means that consecutive day images are shifted by 15.25° in Carrington longitude. For each day, the full-disk Doppler images are divided into 189 overlapping regions covering the solar disk within ±60° in latitude and central meridian distance (CMD) and each region covers a $16^\circ \times 16^\circ$ domain in the transverse cylindrical projection of the solar sphere around the region center. The centers of the regions are spaced by 7.5° ranging from ±52.5° in latitude and CMD. Each of these regions is tracked throughout the sequence of images using the surface rotation rate (Snodgrass 1984) appropriate for the center of each region as tracking rate, and remapped in latitude and longitude. The tracking rate in terms of linear velocity is of the form $\cos(\theta) * (a_0 + a_2 * \sin^2(\theta) + a_4 * \sin^4(\theta))$ where θ is the latitude. Each of the resulting image cubes has a size of 128×128 pixels in the spatial directions and 1664 pixels in the temporal direction. The tracked image cubes are apodized with a circular function, reducing the effective size to 15°, before being Fourier transformed. The analysis is described in detail in Corbard et al. (2003), and its implementation as the GONG ring-diagram pipeline is described in Hill et al. (2003). For GONG data, simultaneous images from different sites are merged (Toner et al. 2003), and the time series of merged images is analyzed. MDI and GONG data are processed in the same way with the exception of the image-merge step.

In this way, we derive 189 pairs of zonal and meridional velocity at 52 grid points in depth for each 1664-min day. Since the inversion grid points are not all independent and the errors increase rapidly at greater depth, we use 16 depths ranging from 0.6 to 15.8 Mm. We combine these daily flow maps to calculate synoptic flow maps for each depth. In merging the various daily flow maps together, a weighting factor of cosine CMD to the fourth power is used, as in the low resolution maps of magnetic activity created at NSO/Kitt Peak. For a given Carrington longitude, 7 or 8 days can contribute to a synoptic map value at the equator (depending on its even or odd position on the longitude grid) compared to 3 or 4 days at 52.5° latitude. Together with the CMD weighting, the values at 52.5° latitude are averaged over about 70% of the amount of data used for regions from the equator to 37.5° latitude.

In addition, we calculate a residual synoptic flow map in order to focus on the flows near active regions. To remove the large-scale component from the flows, we subtract a low-

order polynomial fit in latitude of the longitudinal average of the flows. For the zonal flows, we subtract a fit of sine latitude to the fourth power to reduce the effect of the difference between the differential rotation rate at a given depth and the surface tracking rate. We also subtract a linear trend to remove any north-south asymmetry that might be caused by image distortion or a potential error in the p-angle estimate. For the meridional flows, we remove a function in latitude that is zero at the equator and at the poles. We choose the derivatives in latitude of the first two even Legendre polynomials ($\partial P_2/\partial\theta$ and $\partial P_4/\partial\theta$) to represent the average meridional flow.

From the daily flow maps, we calculate the divergence of the horizontal flow components and the vertical vorticity component

$$\mathrm{div}\, v \;=\; \frac{\partial v_x}{\partial x} \;+\; \frac{\partial v_y}{\partial y} \tag{1}$$

$$\mathrm{vort}\, v \;=\; \frac{\partial v_y}{\partial x} \;-\; \frac{\partial v_x}{\partial y} \tag{2}$$

where v_x is the zonal and v_y is the meridional flow component. We use $\mathrm{div}\, v$ and $\mathrm{vort}\, v$ to distinguish the components from the complete divergence ($\nabla\,\vec{v}$) and vorticity ($\nabla\,\times\,\vec{v}$). We then calculate synoptic maps of these quantities in the same way as for the velocities. In addition, we calculate the vertical gradients, $\partial v_x/\partial z$ and $\partial v_y/\partial z$, of the horizontal flow components and the corresponding synoptic maps. All quantities are functions of latitude, longitude, and depth.

Using the continuity equation (representing mass conservation), we estimate the vertical velocity component from the measured divergence of the horizontal flow (Scorer 1978; Holton 1979). The continuity equation can be written as follows

$$\frac{\partial \rho}{\partial t} \;+\; \nabla\rho \,\cdot\, \vec{v} + \;\rho \,\cdot\, \nabla\vec{v} \;=\; 0 \tag{3}$$

where ρ is the density and $\vec{v}$ is the 3-dimensional velocity vector. Since each data point represents an average over 1664 minutes, we neglect the term of the temporal density fluctuations. In addition, we assume that any horizontal density variations average out over the area of a dense-pack patch. The density is simply a function of radius. The continuity equation can then be simplified to

$$\frac{\partial v_z}{\partial z} \;+\; \left(\frac{1}{\rho}\,\frac{\partial \rho}{\partial z}\right)\, v_z \;+\mathrm{div}\, v \;=\; 0 \tag{4}$$

where $\mathrm{div}\, v$ is the horizontal flow divergence (Equation 1). This equation has the following solution:

$$v_z(d) \;=\; -\,\frac{1}{\rho}\int_{R_\odot}^{R_\odot - d} \rho\,\mathrm{div}\, v\;\mathrm{d}z \;\;+\;\; v_\odot\frac{\rho_\odot}{\rho} \tag{5}$$

at a depth d where $v_\odot$ and $\rho_\odot$ are vertical velocity and density at the solar surface $R_\odot$. To calculate the vertical velocity component, we use the density from a solar model by Christensen-Dalsgaard et al. (1996) and use as boundary condition that the vertical velocity is zero at the surface ($v_\odot = 0.0$). (For future work, we will try to include surface measurements to check the validity of the boundary condition.) From the error in the divergence measurements we estimate the error of the vertical velocity by repeating the calculation after adding or subtracting the divergence error to the differential equation. To estimate the numerical accuracy, we calculate $\partial v_z(d)/\partial z$ from the derived vertical velocity $v_z(d)$ and calculate the left-hand-side of Equation 4. This residual value of the left-hand side can be interpreted as the difference between the calculated gradient $\partial v_z(d)/\partial z$ and the gradient necessary to fulfill the continuity equation. The solution is then acceptable as long as the residual is smaller than the error of the calculated velocity gradient. We find that the residual-to-error ratio is 0.01 ± 0.02 on average for GONG data and 0.02 ± 0.04 for MDI data. We choose the gradient for this quality check and not the divergence or the velocity itself because the error of the observed divergence leads to the error in the vertical velocity which in turn leads to the error in the gradient.

For a weakly stratified atmosphere, the continuity equation can be further simplified and the vertical velocity is defined as

$$v_z(d) \;=\; -\int_{R_\odot}^{R_\odot - d} \mathrm{div}\, v \; \mathrm{d}z \; . \tag{6}$$

In the next section, we find that the divergence of the horizontal flow components is of the order of 10^{-7} s^{-1}. The density gradient term, $(1/\rho)(\partial\rho/\partial z)$, is about 10^{-7} m^{-1} at a depth of 15.8 Mm and increases to 2×10^{-6} m^{-1} at a depth of 0.6 Mm near the surface. Multiplied by a vertical velocity of the order of 1 m s^{-1} or less, this term is comparable to the divergence and not negligible. However, we can use this estimate and its difference from the value calculated using Equation 4 to judge the influence of the density stratification on the vertical velocity component.

The kinetic helicity of a fluid flow is the integrated scalar product of the velocity field, $\vec{v}$, and the vorticity field, $\nabla \times \vec{v}$ (Moffatt & Tsinober 1992):

$$\mathcal{H} \;=\; \int \vec{v} \;\cdot\; \nabla \times \vec{v} \;\, dV \tag{7}$$

where $\vec{v} \cdot \nabla \times \vec{v}$ is called the helicity density of the flow. The kinetic helicity and its density are pseudoscalar quantities. If the vorticity is a stationary random quantity (for example, homogeneous turbulence), one can define the mean helicity

$$H \;=\; \langle\, \vec{v} \;\cdot\; \nabla \times \vec{v} \,\rangle \tag{8}$$

where the angular brackets indicate either an ensemble average or a space average. We can estimate the mean helicity using the measured horizontal flow components and the vertical component derived from the divergence of the horizontal flows. Since the horizontal flow components represent the average flow in a volume element defined by the horizontal size of each dense pack and the depth extent of the inversion kernels, the resulting scalar product $\vec{v} \cdot \nabla \times \vec{v}$ is already a 'mean' quantity. The mean kinetic helicity is dominated by the effect of the differential rotation. To emphasize the influence of magnetic activity, we calculate it from the residual velocities where the large-scale component of the flows has been removed. The kinetic helicity is the only quantity derived in this study where the separation of the flow into an average and a residual component leads to two cross-terms between these flow components in addition to the average and residual component.

3. Results

3.1. Synoptic Flows

We derive daily flow maps of the horizontal flow components which are then combined to synoptic flow maps. Figure 1 shows two examples of synoptic flow maps at 2 Mm and 7 Mm below the solar surface derived from MDI data, superposed on a synoptic map of magnetic activity derived from GONG magnetograms. The flows at 2 Mm swirl around the active regions with strong zonal and meridional components. The flows at 7 Mm show mainly a strong east-west trend; the rotation rate at this depth is faster than the surface tracking rate. The error bars given for the depth values represent the widths of the inversion kernels.

From these synoptic flow maps, we calculate zonal and meridional flows averaged over one Carrington rotation at different depths ranging from 0.6 to 15.8 Mm. Figure 2 shows the average zonal flow component derived from GONG and MDI data. To emphasize the change in the differential rotation with depth, we subtract the constant term of the low-order fit at each depth. This value increases from –5 m s^{-1} at 0.6 Mm to +40 m s^{-1} at 15.8 Mm for GONG data and from –8 m s^{-1} to 33 m s^{-1} for MDI data with a zero-crossing between 2 and 3 Mm. The increase of the constant term with increasing depth reflects the well-known increase of the rotation rate near the outer shear layer.

The zonal flows at high latitudes show a strong variation with depth. The $\sin^4\theta$ term changes from 54 m s^{-1} at 0.6 Mm to –48 m s^{-1} at 15.8 Mm for GONG data and ranges from 36 m s^{-1} at 0.6 Mm to –49 m s^{-1} at 15.8 Mm for MDI data with a zero crossing between 6 and 7 Mm. This shows that the differential rotation profile changes with depth and that

its latitudinal dependence is increasingly more "differential" with increasing depth. The MDI data show a north-south asymmetry which might be caused by an insufficient p-angle correction.

The panel showing zonal flows at a depth of 7.1 Mm includes the zonal flow at r=0.99$R_\odot$ derived from a global rotation inversion (thick curve) of GONG data for the corresponding time period. The local method distinguishes between the hemispheres, while the global analysis leads to a better resolution in latitude. The flows derived from the ring-diagram analysis are similar to the one at r=0.99$R_\odot$ derived from a global rotation inversion (thick curve) with faster flows near the equator and slower flows at mid-latitude, which is the signature of the so-called torsional oscillations.

Figure 3 shows the meridional flows at the same depths as in Figure 2. Positive/negative values imply a flow in a northern/southern direction. The meridional flows are mainly poleward in each hemisphere. Exceptions are the equatorward flow at high latitudes in the northern hemisphere at depths of 7–12 Mm found in the MDI data and near the surface in the GONG data. GONG and MDI data lead to similar flows at other latitudes and depths. The constant terms of the low-order polynomial fits range from –3 m s^{-1} to –7 m s^{-1} for GONG and –4 m s^{-1} to –8 m s^{-1} for MDI data. The coefficients of the even Legendre derivatives are different for GONG and MDI data as expected from Figure 3. For GONG data, the $\partial P_2/\partial\theta$ term is about –20 m s^{-1} at depths greater than 3 Mm and approaches 0 m s^{-1} near the surface, while for MDI data it is about –25 m s^{-1} near the surface and about –10 m s^{-1} at depths below about 5 Mm. The coefficients of $\partial P_4/\partial\theta$ range between –30 m s^{-1} and 0 m s^{-1} reaching the smallest magnitude near 6 Mm for GONG and near 4 Mm for MDI data.

The counter cell seen in the MDI data agrees with previous results by Haber et al. (2002), but it is not seen in the GONG data. The reason for this difference might be that the GONG observations have less high spatial frequency coverage than the MDI observations (Howe et al. 2003) due to the influence of the Earth's atmosphere. We attempted to correct the GONG images with the observed MTF, as described in Toner et al. (2003). When the image restoration is applied, the counter cell at 7–12 Mm is present in the flows derived from GONG data and the near-surface counter flow disappears. However, the current version of image restoration introduces artifacts in frequency shifts and mode amplitudes. At the time of this study we don't know the reason for these artifacts and can thus not rule out that the procedure introduces artifacts in the flows as well. Therefore, we present in this study only GONG results without image restoration applied.

3.2. Divergence and Vertical Velocity

From the daily flow maps, we calculate daily maps of the divergence of the horizontal flow components and combine them to create synoptic maps. Figure 4 shows a synoptic map of the divergence of the horizontal flow components at 7 Mm (see Figure 1(b)) for MDI and GONG as a function of latitude and Carrington longitude. The divergence maps derived from MDI and GONG data are very similar with differences occuring mainly at high latitudes as expected from differences especially in the meridional flow component (see Figure 3). The equatorial region shows predominantly source terms representing upflows, while the region near 20^o latitude shows sink terms or downflows associated with active regions.

Figure 5 shows the longitudinal average of the divergence as a function of latitude and depth. GONG and MDI show positive values (source term) near the equator representing upflows and negative ones (sink term) near 20^o latitude representing downflows. As in the synoptic maps, the downflows appear at locations of large magnetic flux. At high latitudes in the northern hemisphere, the counter flow seen in MDI data results in large negative values at depths greater than 6 Mm which are not seen in GONG data. However, flows are more difficult to measure at high latitudes and, as a consequence, the derived values are less reliable. To emphasize the influence of magnetic activity, we reduce the effect of large-scale flows by fitting and removing a low-order polynomial in latitude (see Figures 2 and 3) and calculate the divergence of the residual flows. The resulting divergence leads to the same pattern but it is shifted toward more negative values.

With the continuity equation (Eq. 4) and the divergence values of the measured horizontal flow components, we calculate the vertical velocity component for each daily map and combine them to synoptic maps. Figure 6 shows, as examples, the vertical velocity at a depth of 7 and 13 Mm derived from GONG data where the large-scale component of the flows has been removed. At a given depth, the vertical flow component shows upflows and downflows at the same horizontal locations where sources and sinks are present in the corresponding divergence map. Locations of strong magnetic activity are more likely associated with downflows at a depth of 7 Mm (top panel), while they show up- or downflows with a slight dominance of upflows at greater depth (bottom panel). Downflows are present at medium flux levels near 20^o latitude at all depths.

The MDI data lead to the same results. The correlation between vertical velocities derived from GONG and MDI data is 0.78 ± 0.04 on average for depths up to 3 Mm and 0.48 ± 0.10 for depths greater than 8 Mm. The reduced correlation at greater depth is due to the presence of the counter cell in the northern hemisphere in the MDI data. By excluding latitudes poleward of 30^o in the northern hemisphere, the correlation nearly doubles to 0.80 ± 0.01 below 8 Mm. Even near the surface, the correlation increases to 0.87 ± 0.05 indicating

that the values at poleward latitudes are more uncertain than values at equatorward ones.

Figure 7 shows the longitudinal average of the vertical velocity. It is qualitatively very similar to the average divergence shown in the 3rd panel of Figure 5. However, the vertical velocity shows large values at greater depth, while the divergence shows large values also near the surface. This difference is especially noticeable near the equator.

Figure 8 shows examples of the vertical velocity as a function of depth at four different latitude-longitude positions. Velocities derived from GONG and MDI data show the same depth dependence but differ quantitatively at depths greater than about 10 Mm. The four cases are representative of the different depth dependences present in the data. For comparison, we include the vertical velocity component (dashed line) derived from MDI data without including the density gradient term in the continuity equation (Equation 6). The consequence of neglecting the density stratification is a vertical velocity that is qualitatively similar but by a factor of two to three too large.

To explore the relationship between vertical velocity and magnetic flux, we group the data into ranges of different magnetic flux and calculate the average vertical velocity for a given range of flux values. Figure 9 shows the average vertical velocity for locations with less than the median flux, six times the median flux, and the range in between as a function of depth averaged over all latitudes within $\pm 37.5^{\circ}$ and all Carrington longitudes. Locations of low magnetic flux (dashed line) show upflows on average, while locations of medium magnetic activity (dotted line) show downflows. Locations of very high activity (solid line) show even larger downflows at depths less than about 8 Mm. The vertical velocity is anticorrelated with the magnetic flux with a correlation coefficient of -0.33 ± 0.04 for GONG data and -0.37 ± 0.04 for MDI data at depths less than 8 Mm.

However, at depths greater than about 10 Mm large upflows occur at some locations with magnetic flux greater than six times the median flux (see Figure 8) which results in an average upflow in GONG data and a greatly reduced downflow in MDI data. The correlation coefficient is +0.11 for GONG and –0.05 for MDI data at a depth of 15.8 Mm. This seems to imply that the vertical flow can change direction at locations of strong activity. But, at the same locations, there is a surprisingly strong correlation between the magnetic activity and the error of the horizontal flow components. For MDI data, the average correlation is 0.68 ± 0.10 for high activity data compared to -0.09 ± 0.09 for low and medium activity. For GONG data, the average correlation is 0.48 ± 0.14 for high activity data at depths greater than 9 Mm and 0.12 ± 0.09 closer to the surface compared to -0.25 ± 0.08 for low and medium activity. This correlation is most likely a side effect of the reduced power of the ring spectra in the presence of strong magnetic flux. The power is reduced by about 20% to 30% (Howe et al. 2003) which amounts to a reduced signal-to-noise ratio. The presence of magnetic

fields can also distort the shape of the rings (Hill, Haber, & Zweibel 1996). For example, it can change the contrast along outer rings and the radii of inner rings. While effects such as the varying contrast along a ring are taken into account in the fitting procedure, it is possible that other distortions of the ring shape caused by magnetic fields contribute to the error correlation. Therefore, it is possible that this reversal of the vertical flow at locations of very high activity is an artifact due to the large error corelation at greater depth and the statistically small sample.

3.3. Vorticity and Kinetic Helicity

From the daily flow maps, we also calculate daily maps of the vertical vorticity component and combine them to synoptic maps. Since we focus on the relation between magnetic activity and the horizontal flows, we use the residual flows after subtracting the large-scale components to derive the vorticity component. Figure 10 shows, the synoptic map of the vertical vorticity component averaged over depth. The maps constructed from GONG and MDI data are again very similar; differences occur mainly at high latitudes. The correlation between vorticity values derived from GONG and MDI synoptic maps for each depth is 0.78 ± 0.05 on average. It increases to 0.89 ± 0.35 when the correlation is restricted to regions equatorward of $45^{\rm o}$ latitude. As a pseudo-vector, the vorticity changes sign at the equator. At locations of strong activity there is a slight preference for the vorticity to be positive in the northern hemisphere and negative in the southern hemisphere. The correlation between magnetic flux and vorticity is only 0.12 ± 0.01 on average for all depths. To calculate the correlation, we changed the sign of vorticity in the southern hemisphere. The correlation changes to 0.17 ± 0.01 at depths less than 3 Mm when the calculation is restricted to regions equatorward of $45^{\rm o}$ latitude but remains at 0.11 ± 0.004 at depths greater than 8 Mm. In the synoptic maps, the correlation between magnetic flux and vorticity is much smaller in magnitude than the corresponding correlation between flux and divergence or vertical velocity.

As shown in Figure 11, the longitudinal average of the vertical vorticity component derived from MDI data shows hardly any variation with depth. Near $20^{\rm o}$ latitude the vorticity is positive on average in the northern hemisphere and negative in the southern, while the sign is reversed near $40^{\rm o}$ latitude. The corresponding plot of GONG data (not included) shows the same behavior.

The vertical vorticity calculated from the average flow (including differential rotation) is negative throughout the southern hemisphere and positive in the northern one at all depths with values ranging from -1.1×10^{-6} s^{-1} to 1.0×10^{-6} s^{-1}. The vorticity of the mean

flow is about one order of magnitude larger than the vorticity of the residual flow. In each hemisphere, its sign is the same as the one of the residual vorticity near 20^o latitude. This implies that the presence of magnetic activity leads to an excess vorticity of the same sign as the one introduced by the rotation. The vorticity of opposite sign at high latitudes in Figure 11 might then simply indicate that we need to remove an additional trend in latitude to completely separate the vorticity into average and residual components.

Figure 12 shows a synoptic map of the kinetic helicity of the residual flow at a depth of 7 Mm derived from MDI data. The GONG data (not shown here) lead to a similar synoptic map. As throughout this study, differences between GONG and MDI data occur mainly at high latitudes. Locations of strong activity show large positive or negative values of helicity. The unsigned helicity is correlated with the unsigned magnetic flux with an average coefficient of 0.28 ± 0.03 for MDI and 0.24 ± 0.05 for GONG data at depths greater than 2 Mm.

3.4. Vertical Gradients of Horizontal Flows

From global helioseismology, it is well-known that the rotation rate decreases from the location of the shear layer near $0.95R_\odot$ toward the solar surface. For this reason, we expect the vertical gradient of rotation to be negative at depths observable with this study. As seen in Figure 13, the vertical gradient of the zonal flow averaged over longitude shows the expected behavior at depths greater than 2 Mm. The negative gradient is stronger at latitudes equatorward of about 25^o than at higher latitudes. Within 2 Mm of the surface at latitudes poleward of about 20^o the gradient reverses its sign indicating an increase of the rotation rate toward the surface. The sign reversal of the gradient at high latitudes agrees with previous observations (Basu, Antia, & Tripathy 1999; Corbard & Thompson 2002).

To study this sign reversal in more detail, we calculate synoptic maps of the gradient at different depths. Figure 14 shows synoptic maps of the vertical gradient of the zonal flows averaged over three different depth ranges. Near the surface (top panel) locations with positive gradient alternate with locations with negative gradient at a given latitude. The positive gradient seen in the longitudinal average is a net result and does not reflect a uniform distribution. At greater depths (mid- and bottom pane), the vertical gradient is predominantly negative. But, there are some locations at high latitudes that show a positive gradient. The most surprising feature is that the vertical gradient appears to track the distribution of magnetic activity. The correlation between magnetic flux and vertical gradient is on average -0.24 ± 0.07 for MDI and -0.24 ± 0.02 for GONG data over all depths which makes it significant almost at the 99.9% level.

Figure 15 shows the vertical gradient of the meridional flow averaged over Carrington longitude derived from MDI data. We calculate this gradient from the absolute values to ensure that it reflects the change in magnitude and not a change in direction. At depths greater than about 7 Mm, the gradient is mainly negative except near the equator and near about 25^o latitude in the northern hemisphere. Large negative gradients occur near $20^o - 30^o$ latitude. The large negative values at latitudes poleward of about 45^o are due to the counter cell. Closer to the surface, the gradient is mainly positive except very close to the surface near the equator and at high latitudes. The GONG data show a similar behavior with the same clear distinction between near-surface and deeper layers.

4. Summary and Discussion

Flow maps are the basic product of a ring-diagram analysis. While they show the complex behavior of the horizontal flows, other tools might be necessary to eventually quantify the dynamics of the flows and their interaction with magnetic activity. For this purpose, we start exploring the use of fluid dynamics descriptors. These descriptors involve, in general, derivatives of the velocity field and not just the velocity itself. We show that we can derive such quantities from flow maps created from MDI and GONG data.

We derive the vertical velocity component of the flow field by assuming mass conservation as stated in the continuity equation. This is an important step since the ring-diagram analysis so far measures only the horizontal flow components. It would be of great interest if it would be possible to derive the vertical velocity directly from the ring-diagram analysis. We find that during the Carrington rotation analyzed in this study the vertical velocity is anticorrelated with magnetic activity. Locations of weak magnetic flux show mainly upflows, while locations of strong magnetic activity show downflows. This agrees with Zhao & Kosovichev (2003a) who found downflows near a sunspot from a time-distance analysis of MDI data. We also find that the vertical velocity can change direction near a depth of about 8 Mm when the magnetic flux is very strong. This might be an artifact introduced by error correlation, as discussed in §3.2. However, it is interesting that Zhao & Kosovichev (2003a) find a similar reversal of the vertical flow in their time-distance analysis of a sunspot.

The small-scale component of the vertical vorticity shows a correlation with magnetic flux. The presence of magnetic activity leads to an excess vorticity of the same sign as the one introduced by the differential rotation. The small-scale component of helicity is large at locations of strong magnetic activity. This agrees with Zhao & Kosovichev (2003b) who found that the residual vorticity peaks in the activity belts and is of opposite sign in each hemisphere from a time-distance analysis of MDI data. Since magnetic activity occurs

mainly between 10^o and 20^o latitude in the analyzed time period, this result agrees also with the latitudinal distribution of helicity derived from sunspot observations by Pevtsov, Canfield, & Metcalf (1995) who used magnetograms covering a much longer time period from 1988 to 1994. We will study the mean kinetic helicity in greater detail when we have more than one Carrington rotation analyzed.

The vertical gradient of the zonal flow shows, as expected, that the rotation rate decreases with increasing radius near the solar surface. We also confirm the sign reversal near the surface at high latitudes previously observed by Basu, Antia, & Tripathy (1999) and Corbard & Thompson (2002). To our surprise, we find that the negative gradient is stronger at locations of large magnetic flux. The vertical gradient of the absolute value of the meridional flow is mainly negative at depths greater than about 7 Mm and mainly positive closer to the surface.

The results shown in this paper are promising but they should not be overinterpreted since the observations cover only one Carrington rotation. From this limited sample, we cannot distinguish whether a result is due to flow dynamics or magnetic activity. For example, the correlation between magnetic flux and the vertical gradient of the zonal flow could just be a coincidence. The latitudinal distribution of the gradient could be time-independent, and we happen to observe during a phase of the solar cycle when magnetic activity is present at low latitudes. The similarity of the results derived from GONG and MDI data gives some confidence in the results since the two different data sets have different systematics. But, both data sets were analyzed with the same ring-diagram pipeline and the GONG pipeline is still being improved. Systematic effects caused by the analysis pipeline would be present in either data set.

As a next step, we intend to analyze data covering a range of activity levels in order to distinguish between the effect of flow dynamics and magnetic activity. For this purpose, we plan to analyze more MDI Dynamics Program data which cover the solar cycle from the previous minimum to the current maximum and declining phase. When the GONG data taken with the upgraded system become available, we will have a continuous data set to analyze covering July 2001 to the present.

Acknowledgments

This work was supported by NASA grants S-92698-F and NAG 5-11703. This work utilizes data obtained by the Global Oscillation Network Group (GONG) project, managed by the National Solar Observatory, which is operated by AURA, Inc. under a cooperative agreement with the National Science Foundation. The data were acquired by instruments operated by the Big Bear Solar Observatory, High Altitude Observatory, Learmonth Solar Observatory, Udaipur Solar Observatory, Instituto de Astrofísico de Canarias, and Cerro Tololo Interamerican Observatory. The SOI–MDI project is supported by NASA grant NAG 5-3077 to Stanford University, with subcontracts to Lockheed Martin, to University of Colorado, and to Harvard University. SOHO is a mission of international cooperation between ESA and NASA. NSO/Kitt Peak data used here are produced cooperatively by NSF/NOAO, NASA/GSFC, and NOAA/SEL. The ring-fitting analysis is based on algorithms developed by Haber, Hindman, and Larsen with support from NASA and Stanford University.

REFERENCES

Basu, Antia, & Tripathy, 1999, ApJ, 512, 458

Bogart, R.S., Sá, L.A.D., Duvall, T.L., Jr., Haber, D.A., Toomre, J., & Hill, F. 1995, in Proc. 4th SOHO Workshop: Helioseismology, vol. 2ed J.T. Hoeksama, V. Domingo, B. Fleck, & B. Battrick (ESA SP-376; Nordwijk: ESA), 147

Bogart, R. et al., 2003, 34th SPD meeting, #08.04

Christensen-Dalsgaard, J. et al., 1996, Science, 272, 1286

Corbard, T. & Thompson, M. 2002, Sol. Phys., 205, 211

Corbard, T., Toner, C., Hill, F., Hanna, K.D., Haber, D.A., Hindman, B.W., & Bogart, R.S. 2003, Local and Global Helioseismology: The Present and Future (Ed. H. Sawaya-Lacoste), ESA SP-517, ESA Publications Division, Noordwijk, The Netherlands, 2003, 255

Dikpati, M. & Gilman, P. 2001, ApJ, 559, 428

Gough, D.O. & Toomre, J. 1983, Sol. Phys., 82, 401

Haber, D.A., Zweibel, E.G., Toomre, J., Bogart, R.S., Sá, L.A.D., Burnette, A., & Hill, F. 1996, Proc. Symposium IAU 181: Sounding solar and stellar interiors (Eds. J. Provost & F.-X. Schmider), Nice, France, 175

Haber, D.A., Hindman, B.W., Toomre, J., Bogart, R.S., Thompson, M.J., & Hill, F. 2000, Sol. Phys., 192, 335

Haber D.A., Hindman, B.W., Toomre, J., Bogart, R.S., Larsen, R.M., & Hill, F. 2002, ApJ, 570, 885

Hill, F. 1988, ApJ, 339, 996

Hill, F., Bolding, J., Toner, C., Corbard, T., Wampler, S., Goodrich, B., Goodrich, J., Eliason, P., & Hanna, K.D. 2003, Local and Global Helioseismology: The Present and Future (Ed. H. Sawaya-Lacoste), ESA SP-517, ESA Publications Division, Noordwijk, The Netherlands, 2003, 295

Hill, F., Haber, D.A., & Zweibel, E.G. 1996, Proc. Symposium IAU 181: Sounding solar and stellar interiors (Eds. J. Provost & F.-X. Schmider), Nice, France, 181

Holton J.R., 1979, An Introduction to Dynamic Meteorology, Academic Press, New York

Howe, R., Komm, R.W., Hill, F., Haber, D.A., & Hindman, B.W. 2003, ApJ(submitted)

Kleeorin, N. & Rogachevskii, I. 2003, Phys. Rev. E, 67, 026321

Krause, F. 1967, Habilitationsschrift, University of Jena

Moffatt, H.K. & Tsinober, A. 1992, Ann. Rev. Fluid Mech., 24, 281

Pevtsov, A.A., Canfield, R.C., & Metcalf, T.R. 1995, ApJ, 440, L109

Scorer, R.S. 1978, Environmental Aerodynamics, Ellis Horwood, Chichester, England

Snodgrass, H.B. 1984, Sol. Phys., 94, 13

Steenbeck, M. & Krause, F. 1966, Z. Naturforschung, 21a, 1285

Toner, C., Haber, D.A., Corbard, T., Bogart, R.S., & Hindman, B.W. 2003, Local and Global Helioseismology: The Present and Future (Ed. H. Sawaya-Lacoste), ESA SP-517, ESA Publications Division, Noordwijk, The Netherlands, 2003, 405

Zhao, J. & Kosovichev, A.G. 2003a, ApJ, 591, 446

Zhao, J. & Kosovichev, A.G., 2003b, 34th SPD meeting, #26.09

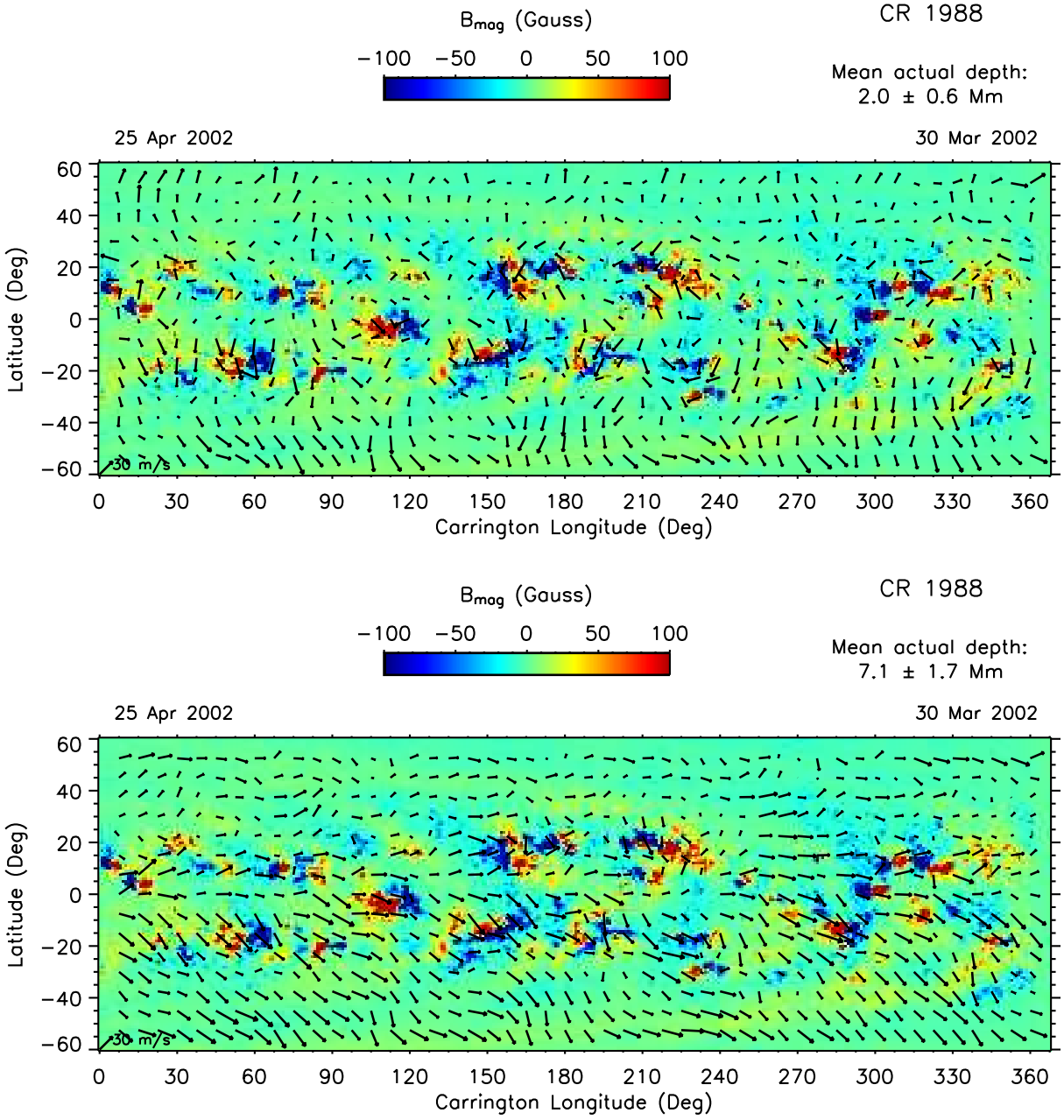

Fig. 1.— *Top:* Synoptic flow map at 2 Mm below the solar surface derived from MDI Dynamics data, superposed on synoptic magnetic data derived from GONG magnetograms. *Bottom:* The same for 7 Mm below the solar surface.

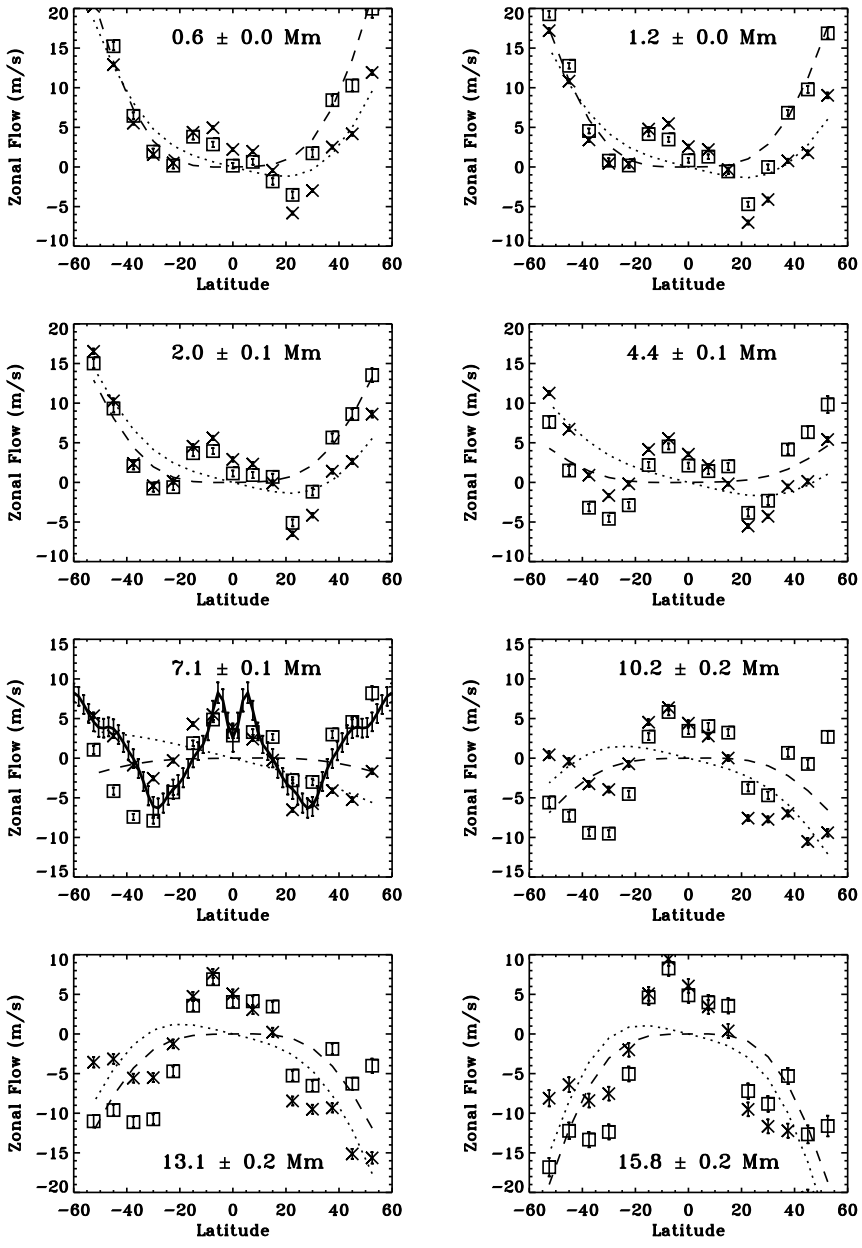

Fig. 2.— The zonal component of the flows averaged in longitude over Carrington rotation CR 1988 (GONG data: square symbols; MDI data: star symbols) at several depths (0.6, 1.2, 2.0, 4.4, 7.1, 10.2, 13.1, 15.8 Mm). The surface rotation rate (tracking rate) has been subtracted. The low-order polynomial fits are included for comparison (GONG data: dashed line; MDI data: dotted line). The fitted equatorial value has been subtracted. The thick curve in the panel at depth 7.1 Mm represents the zonal flow at $0.99R_\odot$ derived from a global rotation inversion.

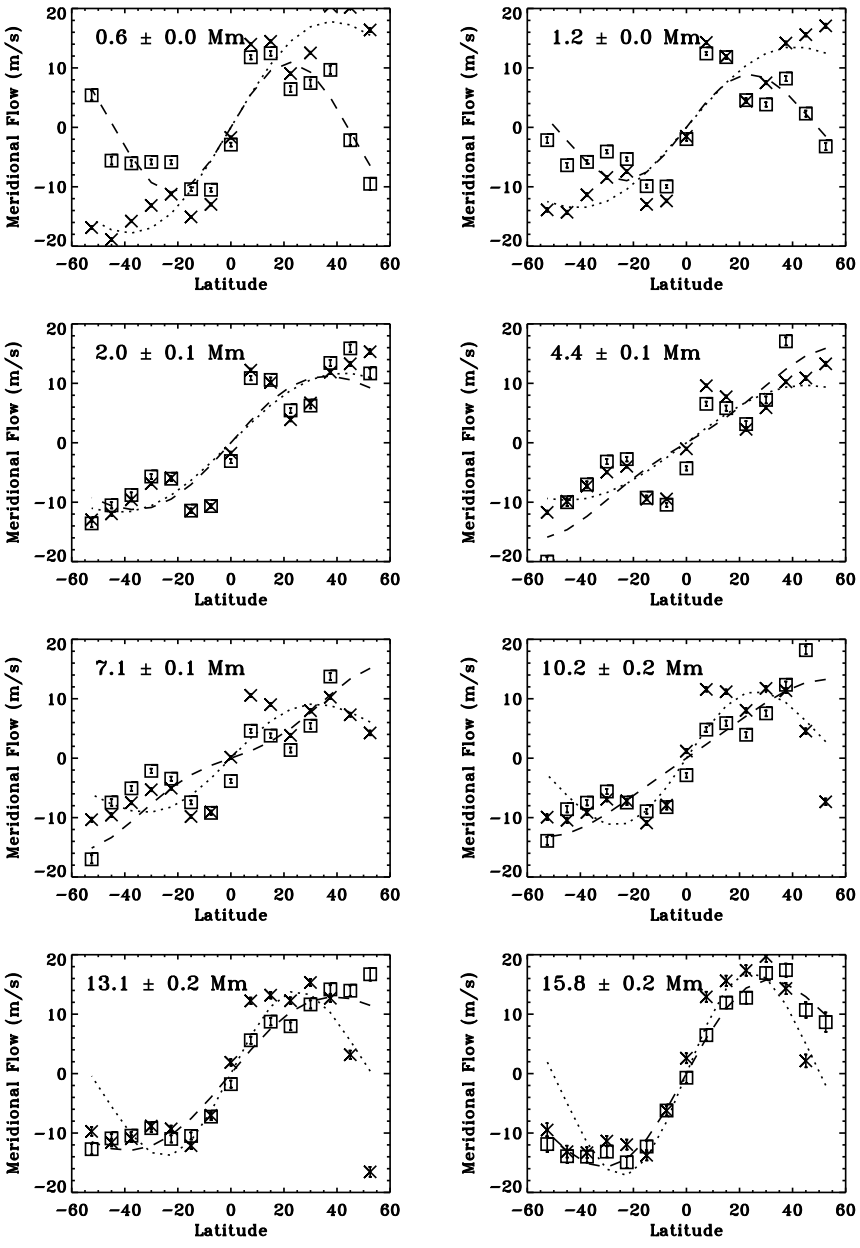

Fig. 3.— Same as Figure 2 for the meridional flow component.

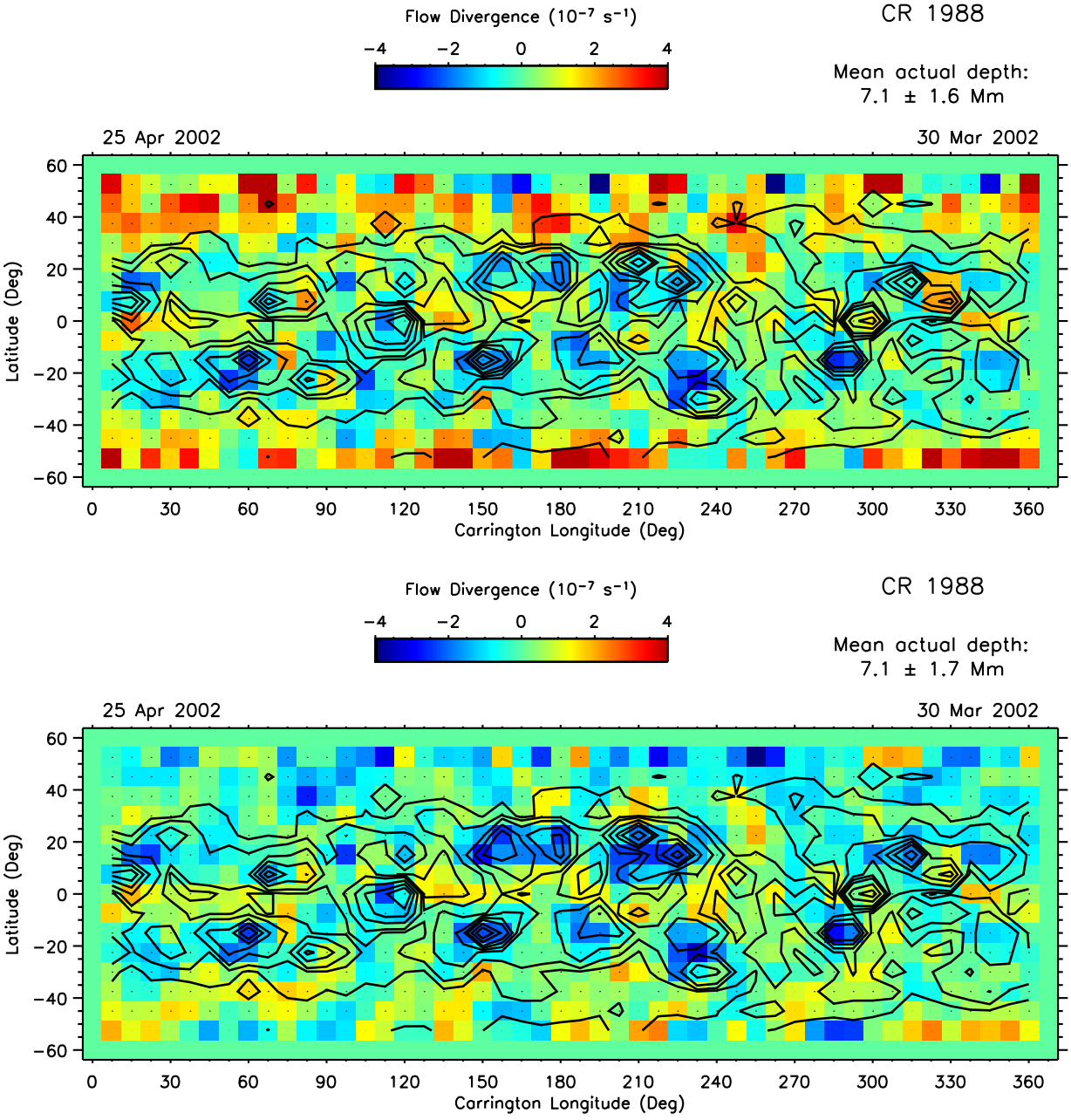

Fig. 4.— *Top:* The divergence of the horizontal flow components at a depth of 7 Mm derived from GONG data. The contour lines indicate the magnetic flux (5, 10, 20, 40, 60, 80, 120, 160 G). *Bottom:* The same for MDI data.

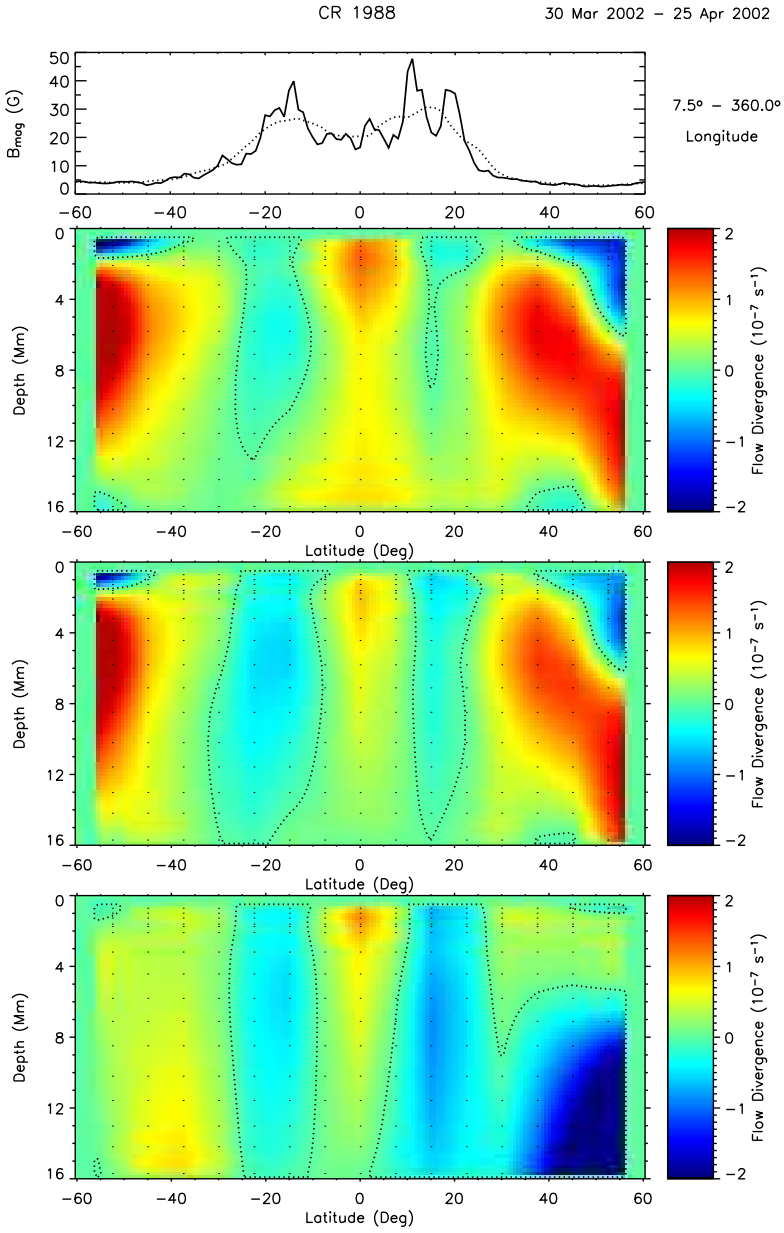

Fig. 5.— The divergence of the horizontal flow components averaged over Carrington rotation CR 1988 as a function of latitude and depth. *Top:* Surface magnetic flux as a function of latitude (solid line) and averaged over 15° (dotted curve). *Second:* Flow divergence derived from GONG data. The dotted line indicates the zero contour. The dots indicate the depth-latitude grid. *Third:* Flow divergence derived from GONG data after removing the low-order polynomial fit. *Bottom:* Same as third panel for MDI data.

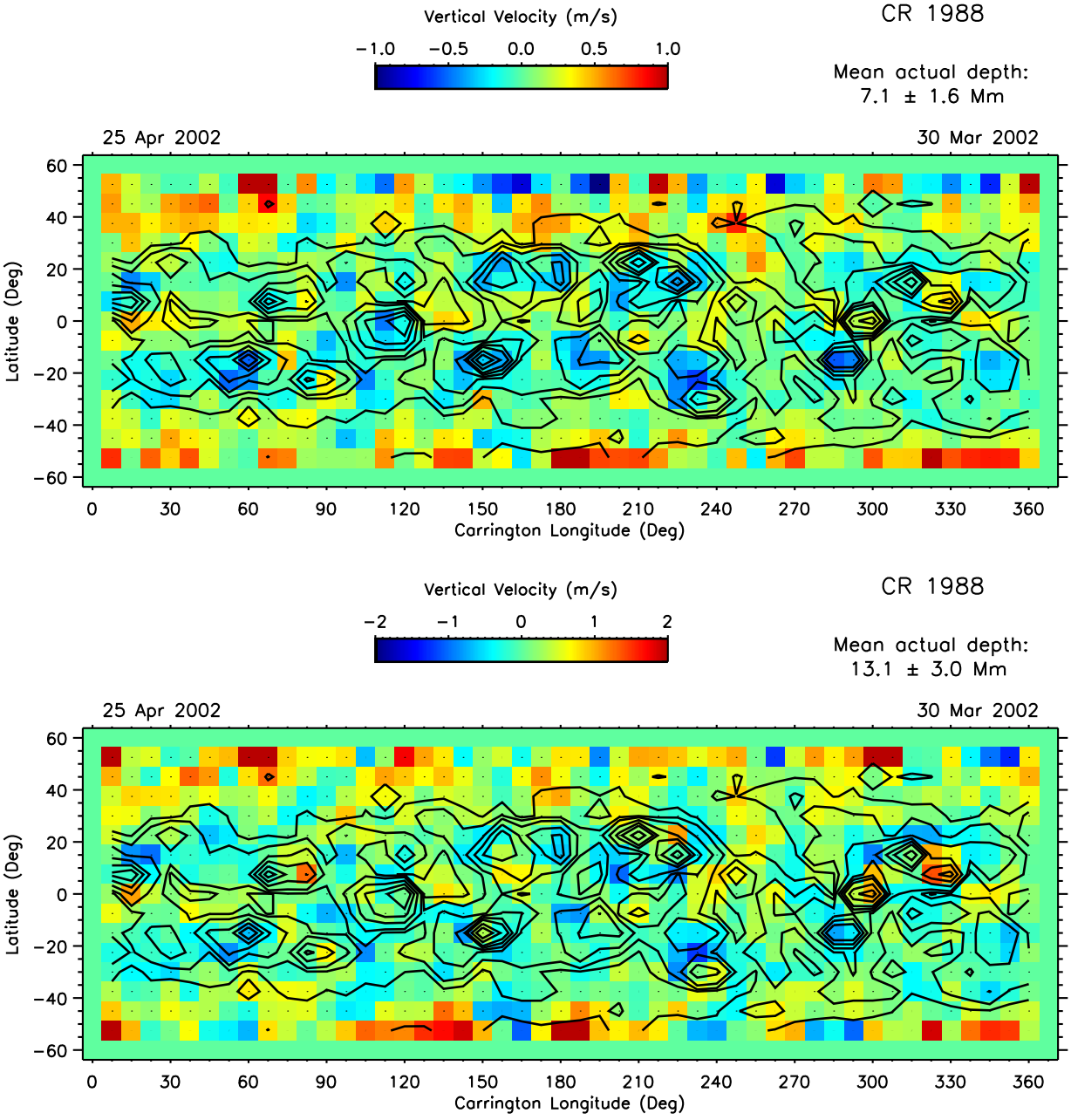

Fig. 6.— *Top:* The vertical velocity at a depth of 7.1 Mm derived from GONG data with low-order polynomial fit removed. The contour lines indicate the magnetic flux (5, 10, 20, 40, 60, 80, 120, 160 G). *Bottom:* The same at a depth of 13.1 Mm.

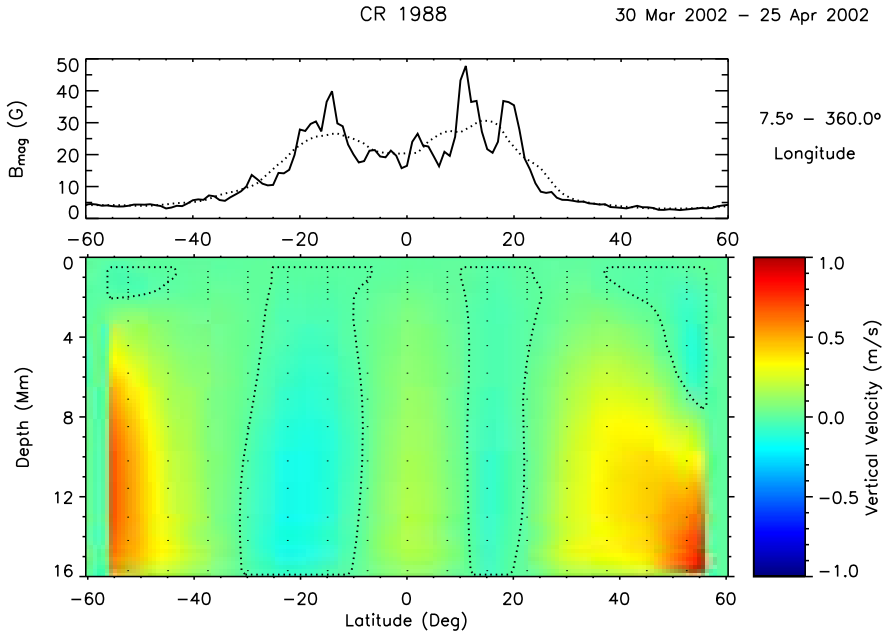

Fig. 7.— The vertical velocity component averaged over Carrington rotation CR 1988 as a function of latitude and depth. *Top:* Surface magnetic flux as a function of latitude (solid line) and averaged over 15° (dotted curve). *Bottom:* Vertical velocity derived from GONG data after removing the low-order polynomial fit. The dotted line indicates the zero contour. The dots indicate the depth-latitude grid.

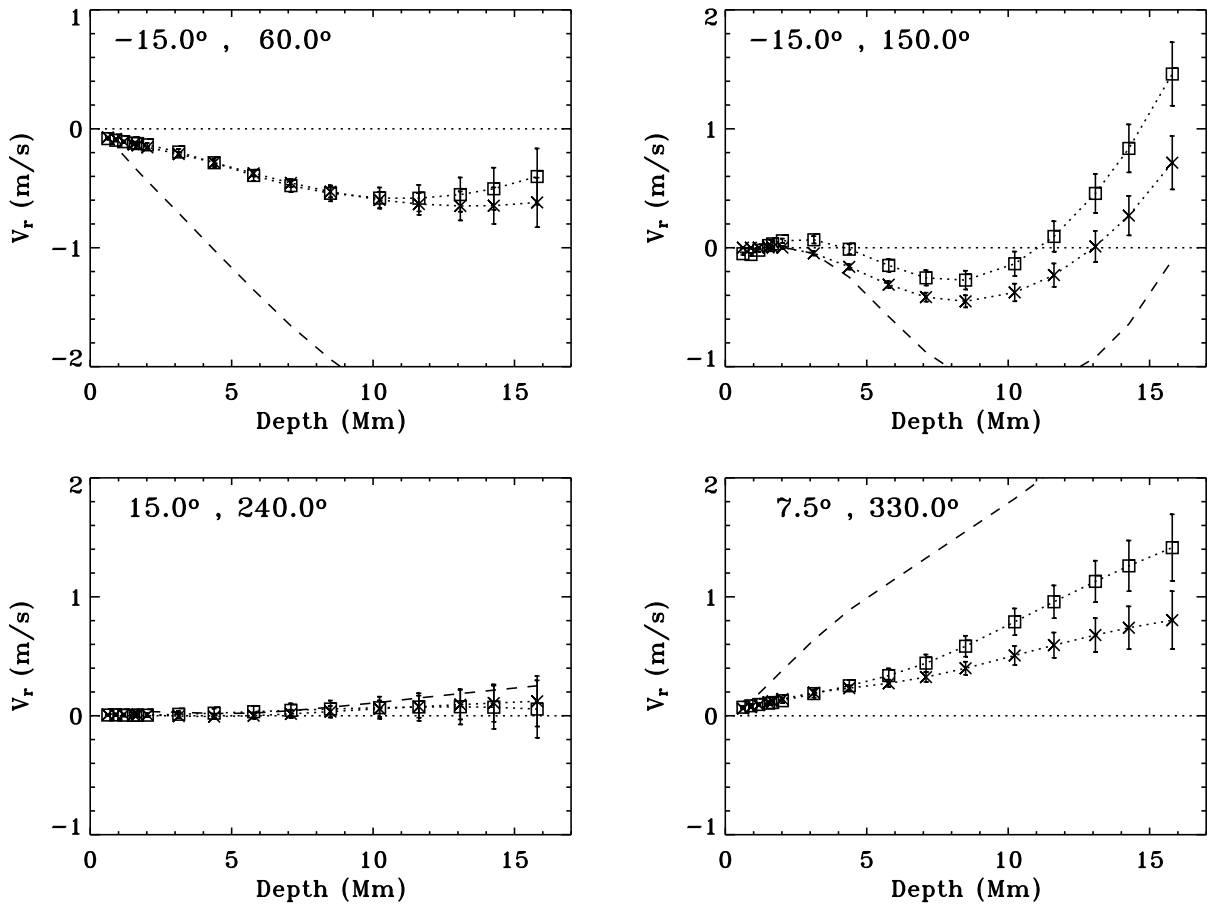

Fig. 8.— The vertical velocity as a function of depth at four different positions in latitude and longitude (GONG data: square symbols; MDI data: star symbols). The low-order polynomial fit was removed. The dashed line indicates the vertical velocity derived from MDI data without including the density gradient.

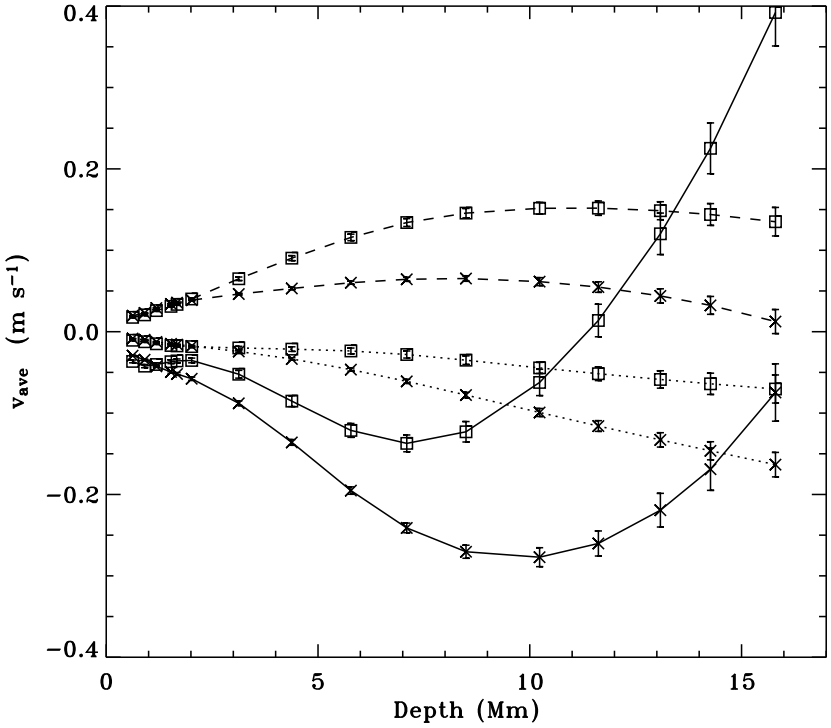

Fig. 9.— The vertical velocity averaged over three different ranges of surface magnetic flux (dashed line: less than median flux of 8.9 G; dotted line: between one and six times the median flux; solid line: greater than six times the median flux) for all longitudes and $\pm 37.5^{\circ}$ latitude for both data sets (GONG data: squares; MDI data: stars).

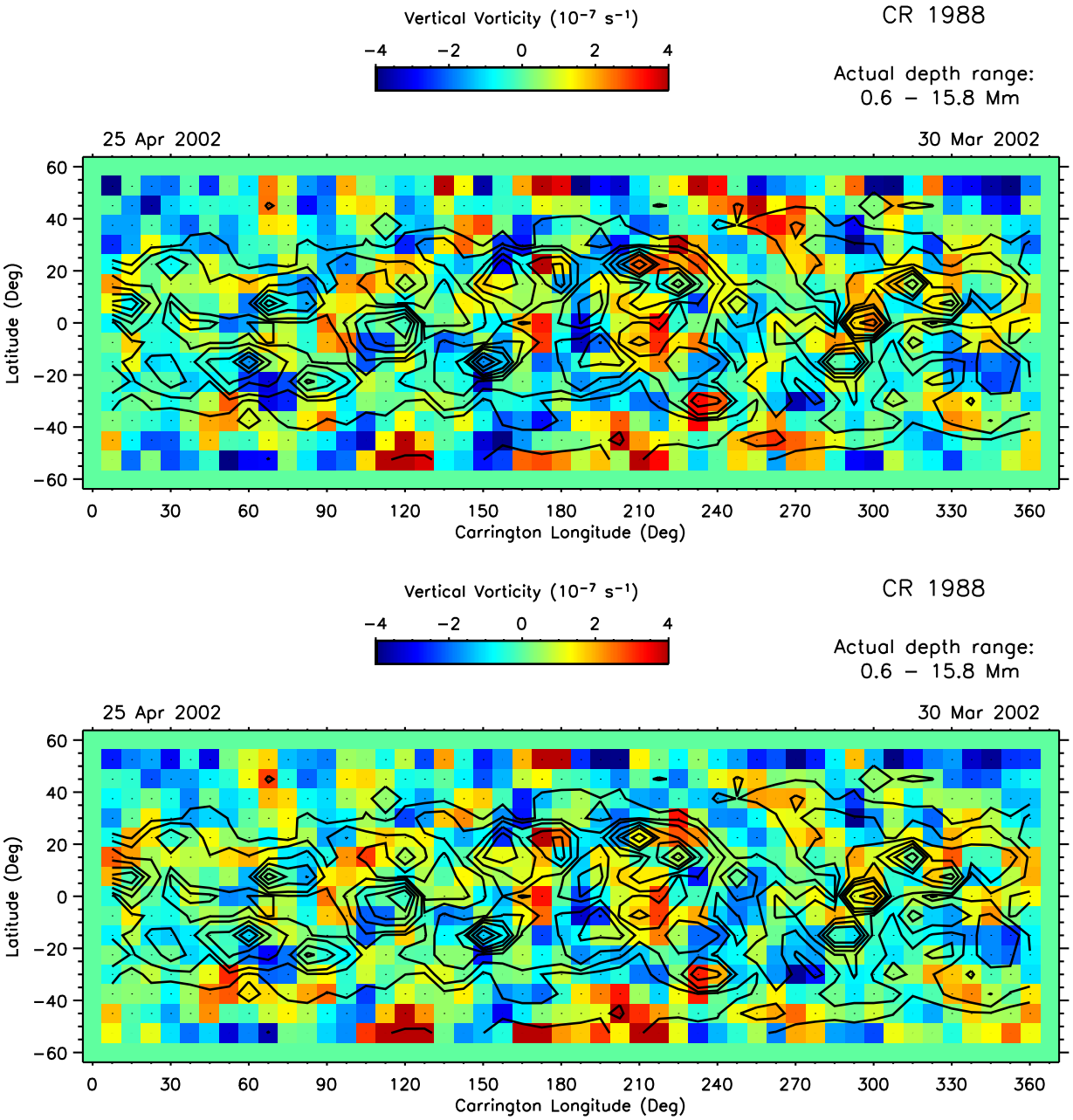

Fig. 10.— Same as Figure 4 for the vertical vorticity component averaged over all depths (*Top:* GONG data, *Bottom:* MDI data.

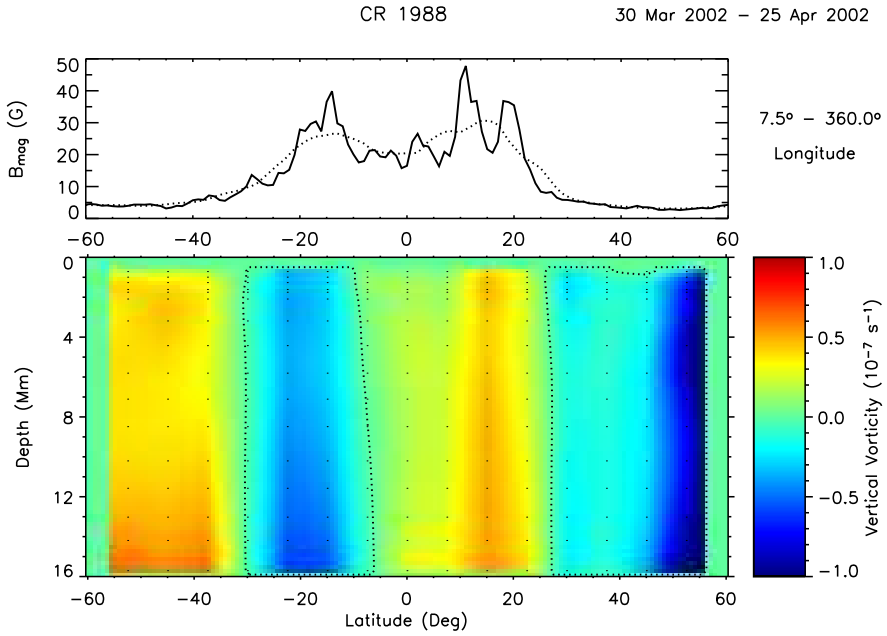

Fig. 11.— Same as Figure 7 for the vertical vorticity component derived from MDI data after removing a low-order polynomial fit.

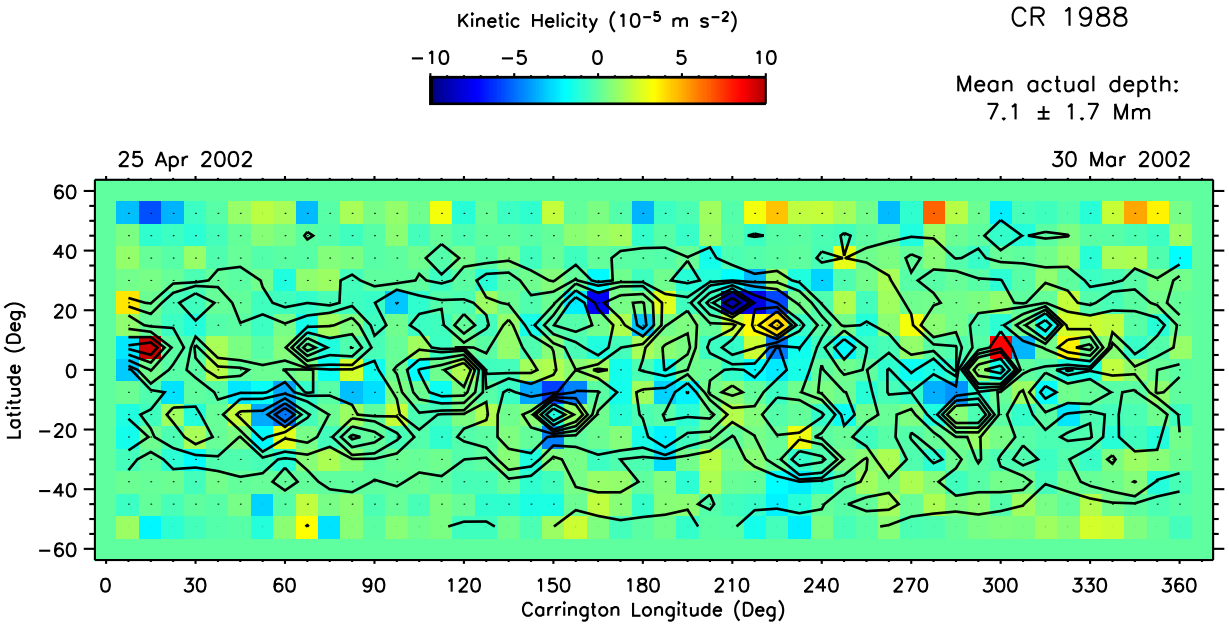

Fig. 12.— The kinetic helicity at a depth of 7 Mm derived from MDI data. The contour lines indicate the magnetic flux (5, 10, 20, 40, 60, 80, 120, 160 G).

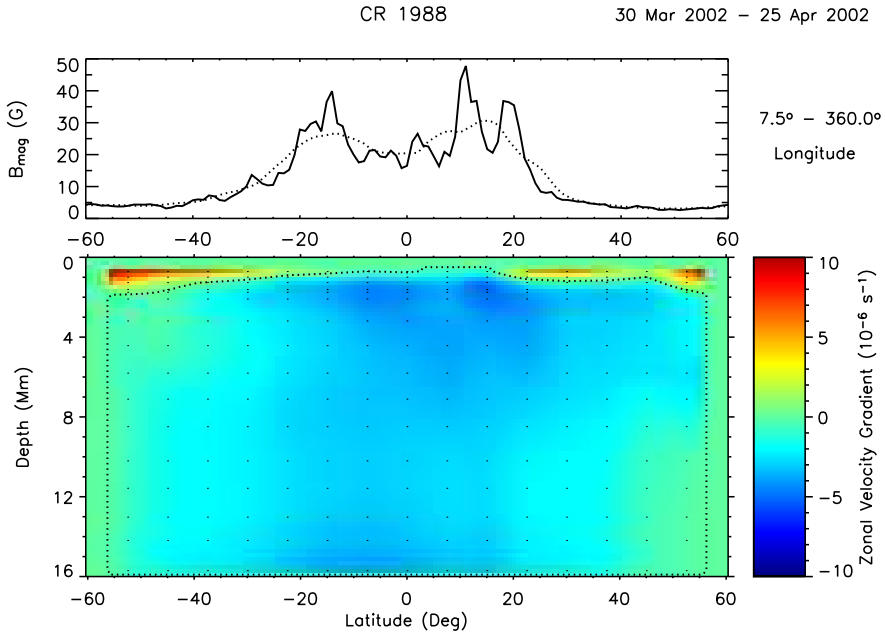

Fig. 13.— Same as Figure 11 for the vertical gradient of the zonal flow derived from GONG data.

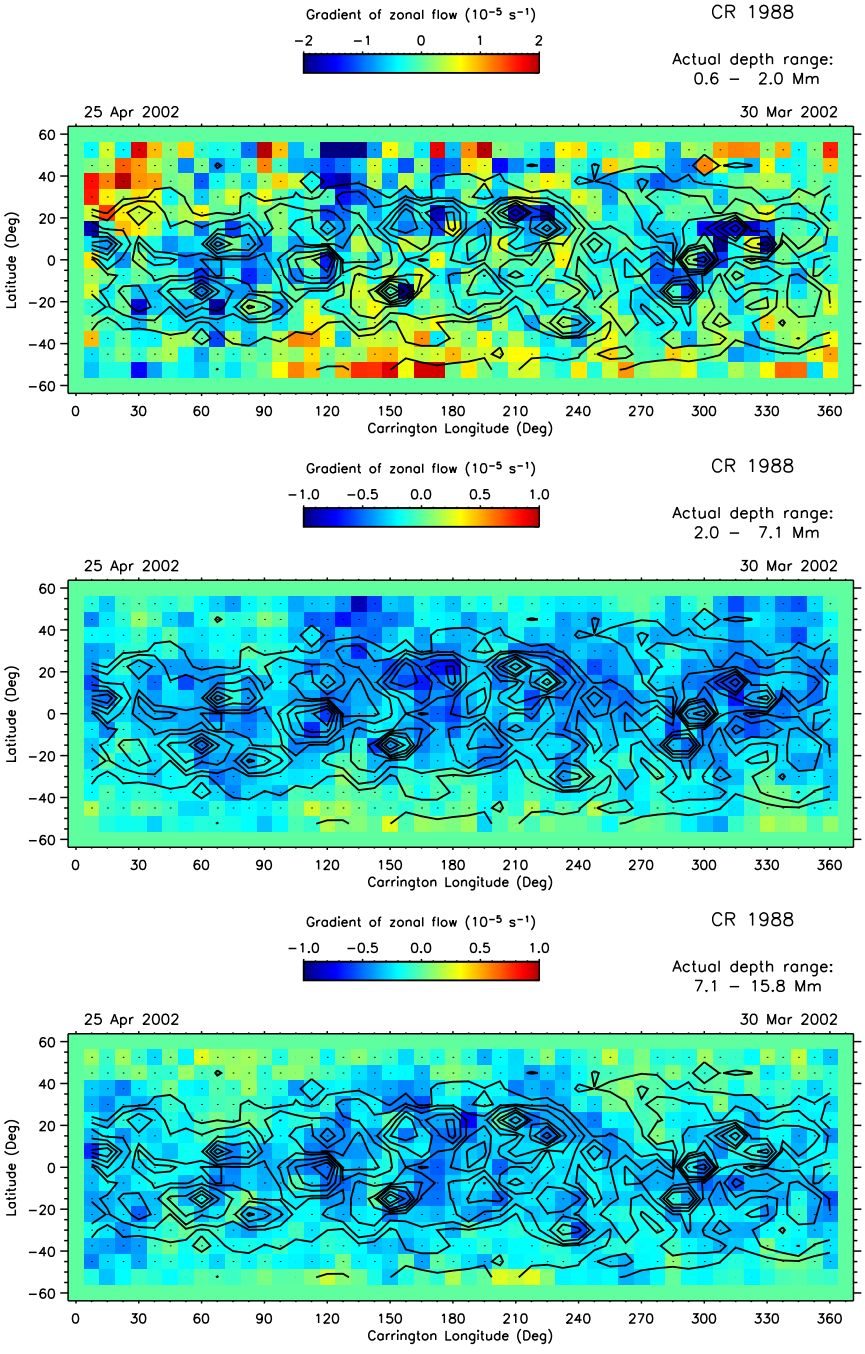

Fig. 14.— The gradient of zonal flows averaged over three depth ranges derived from GONG data. The contour lines indicate the magnetic flux (5, 10, 20, 40, 60, 80, 120, 160 G). *Top:* 0.6–2.0 Mm; *Middle:* 2.0–7.1 Mm; *Bottom:* 7.1–15.8 Mm.

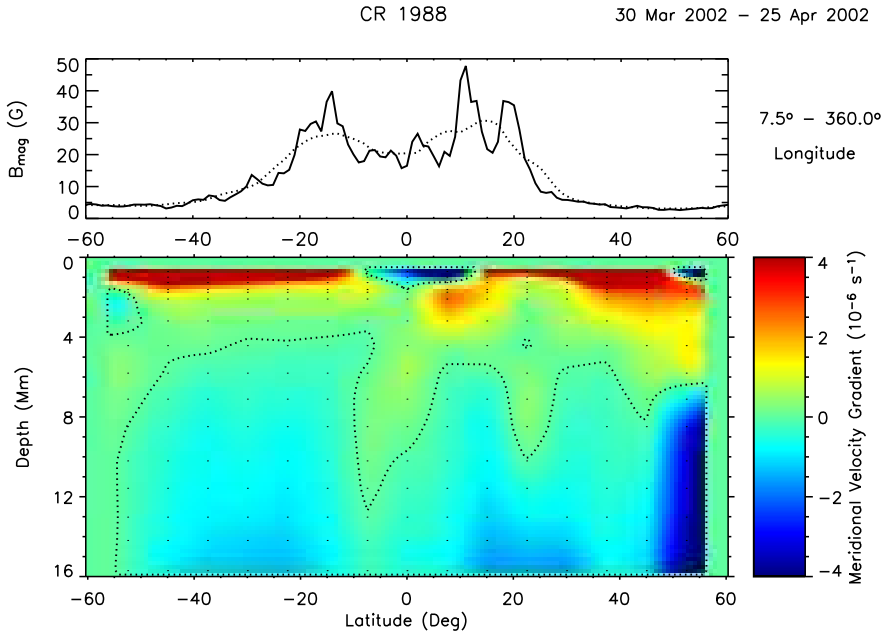

Fig. 15.— Same as Figure 11 for the vertical gradient of the absolute value of the meridional flow derived from MDI data.